Nano Research 2015, 8(2): 554–565
DOI 10.1007/s12274-014-0669-7
Research Article
ISSN 1998-0124
CN 11-5974/O4

One-dimensional manganese borate hydroxide nanorods and the corresponding manganese oxyborate nanorods as promising anodes for lithium ion batteries

Aihua Li, Liqiang Xu (✉), Shouli Li, Yanyan He, Ranran Zhang, and Yanjun Zhai

Key Laboratory of Colloid & Interface Chemistry (Shandong University), Ministry of Education and School of Chemistry and Chemical Engineering, Shandong University, Jinan 250100, China

Received: 14 September 2014
Revised: 21 November 2014
Accepted: 30 November 2014

KEYWORDS
one-dimensional,
manganese borate hydroxide,
manganese oxyborate,
lithium ion battery

ABSTRACT

Novel manganese and boron containing nanomaterials have been investigated for applications in rechargeable lithium ion batteries (LIBs) in recent years owing since they are more environmentally-benign and more abundant in nature than the materials currently employed. In this study, one-dimensional (1D) $Mn_3B_7O_{13}OH$ nanorods and $MnBO_2OH$ nanorod bundles were controllably fabricated by using $NH_4HB_4O_7$ and $Mn(NO_3)_2$ as reagents via a hydrothermal or solvothermal process, respectively, without any surfactants or templates at 220 ˚C. It is interesting to find that both materials are transformed into Mn_2OBO_3 nanorods/nanorod bundles by subsequent calcination. The formation processes of the above 1D borate containing products were investigated and the as-obtained four kinds of borates were studied as novel anode materials. It was found that the Mn_2OBO_3 nanorods displayed the best performance among the four borates, delivering an initial discharge capacitiy of 1,172 mAh·g^{-1} at 100 mA·g^{-1}, and 724 mAh·g^{-1} could be retained after 120 cycles. A full battery composed of a Mn_2OBO_3 nanorod anode and a commercial $LiFePO_4$ (or $LiCoO_2$) cathode has also been assembled for the first time, which delivered an initial discharge capacity of 949 mAh·g^{-1} (779 mAh·g^{-1} for $LiCoO_2$). The excellent cycle and rate performances of the products reveal their potential applications as anodes for LIBs.

1 Introduction

Polyanion-type inorganic compounds as electrode materials display unique advantages (such as the possibility to systematically tune the potentials of transition metal containing electrodes) and are competitive with traditional materials for use in lithium-ion batteries (LIBs) [1, 2]. Among these materials, transition metal borates have attracted increasing research interests since their first utilization as anodes for LIBs in 2001, owing to their advantages of containing the smallest molecular weight polyanion, the high abundance of

Address correspondence to xulq@sdu.edu.cn

precursor materials and being environmental friendly, as well as having high discharge voltage and initial capacity [3]. To date, a series of metal borates have been prepared via diverse methods and applied as anodes. For example, $FeBO_3$, Fe_3BO_6 and Cr_3BO_6 particles were prepared through a solid-state reaction at 600–880 ˚C for 2–5 days with relatively high initial discharge capacity, but capacities of only 250, 450 and 280 mAh·g^{-1} could be maintained after 5–10 cycles [4]; VBO_3 particles prepared by firing a mixture of V_2O_3 and H_3BO_3 at 670 ˚C and 1,200 ˚C for 1 day, respectively, had an initial capacity of 420 mAh·g^{-1}; 20 wt.% carbon-coated VBO_3 gave an initial capacity of 910 mAh·g^{-1}, which faded to 420 mAh·g^{-1} after 12 cycles [5]; $M_3B_2O_6$ (M = Co, Ni, and Cu) particles were fabricated via similar solid-state reactions for 4 days, and their initial capacity was 700 mAh·g^{-1}, and 300 mAh·g^{-1} could be retained after 30–50 cycles [6]. Although extensive research and obvious progress have been made in the synthesis of the above MBO_3 and $M_3B_2O_6$ (M = Fe, Co, Ni, Cr, V and Cu) materials, the time-consuming (at least 2 days) synthesis process and fast capacity fading of these materials have hindered their wider applications.

Manganese is cheaper, more environmentally benign and more abundant in nature than the majority of transition metals [7–10]. Manganese based borates have already been synthesized and investigated in various fields. For example, pyroborate $Mn_2B_2O_5$ has been prepared by a solid state reaction at 1,150 ˚C and its magnetic properties have been investigated using magnetization and electron paramagnetic resonance measurements [11]. In addition, specific heat and magnetization measurements on warwickite Mn_2OBO_3 have been carried out, and the Mn_2OBO_3 displayed L-type ferrimagnetism [12]. The interplay of spin, charge and orbital degrees of freedom in Mn_2OBO_3 is also of great interest and its long range antiferromagnetic order occurs below a Néel temperature T_N = 26 K, other apparent magnetic transitions are due to secondary phases [13]. However, to the best of our knowledge, a convenient synthesis of manganese borate hydroxide and the corresponding manganese oxyborate nanomaterials, especially 1D nanomaterials, for use as high performance anodes for LIBs has not been reported [14].

Herein, a facile hydrothermal/ethanol thermal method has been developed to prepare 1D $Mn_3B_7O_{13}OH$ nanorods and $MnBO_2OH$ nanorod bundles. They can subsequently be converted into Mn_2OBO_3 with similar morphologies via calcination. The as-obtained four kinds of nanomaterials have been systematically investigated as lithium-ion battery anodes for the first time. The $Mn_3B_7O_{13}OH$ nanorods, $MnBO_2OH$ nanorod bundles, Mn_2OBO_3 nanorods and Mn_2OBO_3 nanorod bundles displayed initial discharge capacities of 810, 855, 1,172 and 1,037 mAh·g^{-1}, with capacities of 538, 507, 600 and 554 mAh·g^{-1}, respectively, retained after 50 cycles. The Mn_2OBO_3 nanorods/nanorod bundles delivered higher initial discharge capacities than the corresponding borate hydroxides. Among the four samples, the Mn_2OBO_3 nanorods displayed the best cycle performance and rate performance. The Mn_2OBO_3 nanorods also showed good reversibility and stability upon increasing the discharge/charge current density to 50, 100, 200, 500, and 1,000 mAh·g^{-1}. Notably, after 60 cycles at varying current densities, the discharge capacity of Mn_2OBO_3 nanorods could recover to 784 mAh·g^{-1} when the current density was reset to 50 mA·g^{-1}. In addition, the Mn_2OBO_3 nanorod anode has also been assembled with a commercial $LiFePO_4$ cathode to form a full battery, which showed an initial discharge capacity of 949 mAh·g^{-1}. The excellent electrochemical performance of Mn_2OBO_3 demonstrates its potential as a promising anode for LIBs. This method provides a new general strategy for the synthesis of a series of borate containing materials with promising applications as anodes for LIBs.

2 Experimental

2.1 Material synthesis

In a typical procedure, 0.01 mol $NH_4HB_4O_7{\cdot}3H_2O$ and 0.01 mol $Mn(NO_3)_2$ (50 wt.% solution) were dissolved in 40 mL of distilled water (or ethanol) and then transferred into a 60 mL Teflon-lined stainless-steel autoclave after being stirred vigorously for 1 hour. The autoclave was heated at 220 ˚C and the temperature maintained for 24 h (or 12 h). The resulting precipitates were collected and washed several times ($Mn_3B_7O_{13}OH$ or $MnBO_2OH$). Finally, the corresponding Mn_2OBO_3

materials were obtained by calcining the $Mn_3B_7O_{13}OH$ and $MnBO_2OH$ in air at 750 ℃ with a heating rate of 5 ℃/min for 12 h or 5 h, respectively.

2.2 Characterization

The phase of the as-obtained products were measured on a Bruker D8 Advance X-ray diffractometer equipped with graphite-monochromatized Cu Kα radiation (λ = 1.5418 Å). Transmission electron microscopy (TEM, JEM-2100), field emission scanning electron microscopy (FESEM; JEOL JSM-6700F) and high-resolution TEM (HRTEM, JEM-2100, 200 kV) were used to observe the morphology, size and structure of the samples.

2.3 Battery assembly and electrochemical measurements

The electrochemical behavior of the half batteries were examined using CR2032 coin type cells vs. Li with 1 M $LiPF_6$ dissolved in the solution of ethylene carbonate/dimethyl carbonate/diethyl carbonate (EC/DMC/DEC, 1:1:1 *w*/*w*) as the electrolyte. The working anode electrode was fabricated by compressing a slurry of active materials (70 wt.%), carbon black (20 wt.%), carboxymethyl cellulose III (CMC) (10 wt.%) onto a copper foil current collector and dried under vacuum at 60 ℃ for 12 h. The resulting foil was roll-pressed and cut into discs with a diameter of 12 mm. The typical loading density of the active materials on the discs was 1.5–2.0 mg·cm^{-2}. The cathode electrode was prepared by blending the active material [commercial $LiFePO_4$ (or $LiCoO_2$) powder, 80 wt.%], carbon black (10 wt.%) and CMC (10 wt.%) in water. The slurry was then drop cast onto aluminum foil and dried under vacuum overnight. The resulting foil was roll-pressed and cut into discs with a diameter of 14 mm. The typical loading density of the active materials on the discs was 10–15 mg·cm^{-2}. The assembly of cells was carried out in an argon-filled glove box, where the amount of water and oxygen were both <1 ppm. To assemble the full battery, a Mn_2OBO_3 nanorod anode was combined with a commercial $LiFePO_4$ cathode and assembled into CR2032 coin type cells. The tested cells were cycled on a Land battery test system (CT2001A, China) at room temperature (25 ℃). Cyclic voltammetry (CV) measurements were obtained using a LK2005A Electrochemical Workstation. Electrochemical impedance spectroscopy (EIS) was carried out at 5 mV in the frequency range from 10^{-2} Hz to 10^5 Hz at open-circuit voltage using a MaterialsMates 510 instrument.

3 Results and discussion

The X-ray diffraction peaks of the samples prepared through a hydrothermal or ethanol thermal process shown in Figs. 1(a) and 1(b) can be indexed as pure cubic $Mn_3B_7O_{13}OH$ (JCPDS card no. 28-0645) and $MnBO_2OH$ (JCPDS card no. 47-1864), respectively. The FESEM image (Fig. 1(c)) of the $Mn_3B_7O_{13}OH$ shows that nanorods with lengths in the range of 10–20 micrometers and average diameter of 200 nm have been produced. The $MnBO_2OH$ is mainly composed of nanorod bundles with lengths in the range of 10–15 micrometers and an average diameter of 350 nm (Fig. 1(d)).

It is interesting to find that 1D $Mn_3B_7O_{13}OH$ and $MnBO_2OH$ could all transform into Mn_2OBO_3 after calcination. The phases of the as-synthesized products are determined by XRD and the results are shown in Fig. 2(a). All the diffraction peaks of the two samples can be indexed as monoclinic Mn_2OBO_3 (JCPDS no. 49-1172), and the calculated lattice parameters are consistent with the literature [15]. In term of the solvent used in the first step, we denote the Mn_2OBO_3 derived from $Mn_3B_7O_{13}OH$ and $MnBO_2OH$ as "w-Mn_2OBO_3" and "e-Mn_2OBO_3", respectively. Compared with the reported synthesis method of Mn_2OBO_3, this two-step method is more convenient [12, 13, 16]. The schematic structure of $Mn^{2+}Mn^{3+}OBO_3$ depicted in Fig. 2(b) reveals that the metal cations are octahedrally coordinated, with the octahedra sharing edges to form ribbons, linked by corner sharing, and trigonal planar BO_3 groups are also present [16]. It is worth noting that the phase transition from $Mn_3B_7O_{13}OH$ and $MnBO_2OH$ to w-Mn_2OBO_3 and e-Mn_2OBO_3 was achieved through a one-pot calcination while the one-dimensional characteristics are retained [Figs. 2(c) and 2(d)]. But the w-Mn_2OBO_3 nanorods (0.15–1.0 micrometers) are shorter than those of $Mn_3B_7O_{13}OH$. The e-Mn_2OBO_3 is also composed of shorter nanorods that are cross-linked together to form long nanorods (inset in Fig. 2(d)).

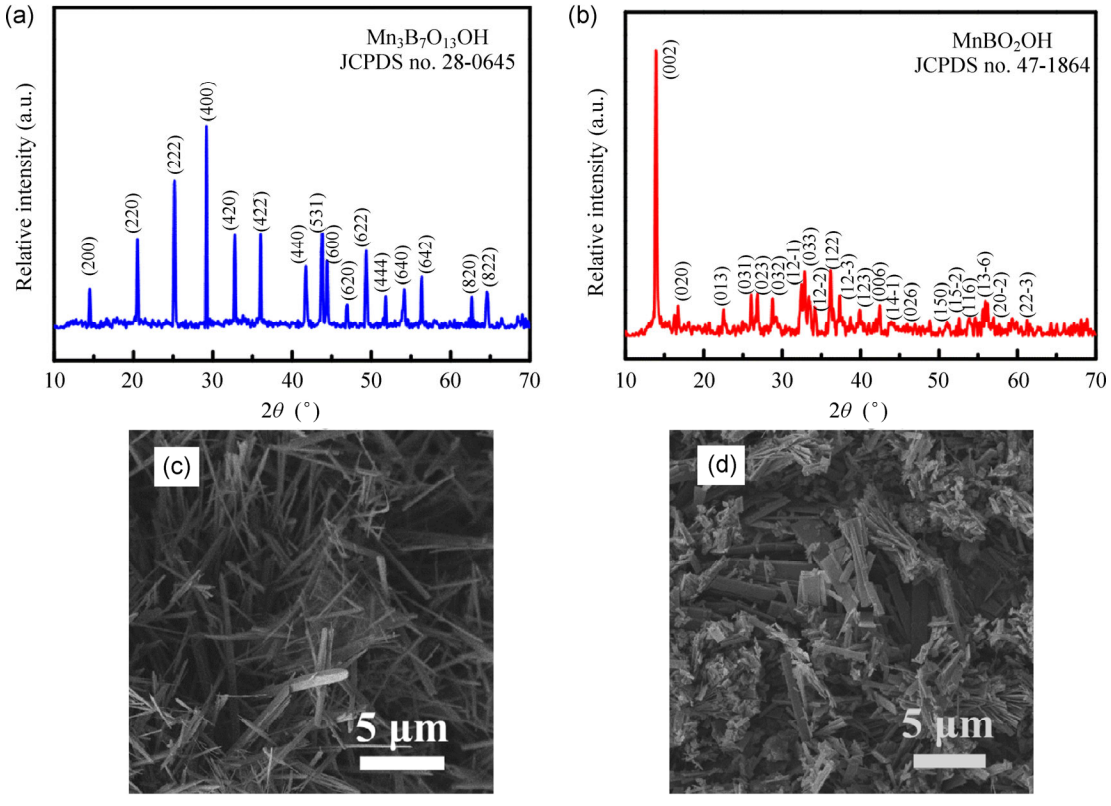

Figure 1 (a, b) XRD patterns and (c, d) FESEM images of $Mn_3B_7O_{13}OH$ and $MnBO_2OH$.

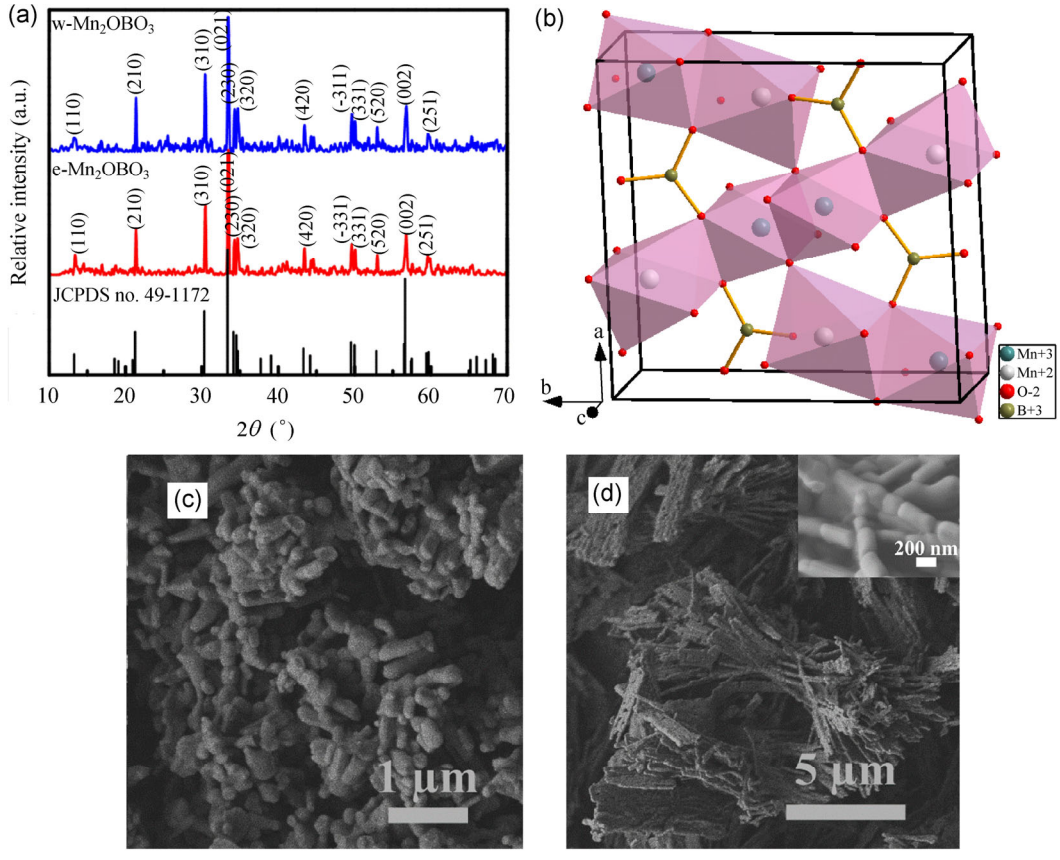

Figure 2 (a) XRD patterns (b) crystal structure and (c, d) FESEM images of the as-obtained Mn_2OBO_3 products.

The structures of the as-obtained w-Mn_2OBO_3 and e-Mn_2OBO_3 were examined by HRTEM (Fig. 3). The HRTEM image in Fig. 3(a) reveals the nanorod shape of w-Mn_2OBO_3. Figure 3(b) shows the regular arrangement of lattice fringes with an average d-spacing of 4.17 Å, which corresponds to the (210) plane of the monoclinic phase of Mn_2OBO_3. Figure 3(c) further shows that e-Mn_2OBO_3 long nanorod is made up of cross-linked short nanorods. The lattice fringes with an average d-spacing of 2.67 Å can be indexed to be the (021) planes of the monoclinic Mn_2OBO_3 (see Fig. 3(d)).

Time-dependent experiments were performed to gain insight into the formation process of these manganese oxyborates. The time-dependent experiments on the formation of $Mn_3B_7O_{13}OH$ and $MnBO_2OH$ were carried out by analyzing TEM images and XRD patterns obtained after different reaction times [Figs. S2 and S3, in the Electronic Supplementary Material (ESM)]. The formation process might include the following stages: (1) nucleation and nanoparticle formation in the initial stages [Figs. S1(a) and S1(e), in the ESM]; (2) aggregation and crystallization processes—from a thermodynamics perspective, the nanoparticles tend to aggregate or assemble together to decrease the overall surface energy. As a result, crystalline MnO_2 rods and $Mn_3B_7O_{13}OH$ particles were formed with increasing reaction time [Figs. S1(b) and S1(f)]; (3) the phase evolution from MnO_2 into $Mn_3B_7O_{13}OH$ might occur on further prolonging the reaction time (as partly evidenced by the XRD pattern, while for ethanol as a solvent, the $Mn_3B_7O_{13}OH$ particles began to assemble into bundles during the phase transformation from $Mn_3B_7O_{13}OH$ into $MnBO_2OH$ [Figs. S1(c) and S1(g)]; (4) oriented growth—subsequently, the $Mn_3B_7O_{13}OH$ nanorods and $MnBO_2OH$ nanorod bundles underwent an oriented growth process to form larger and uniform nanorods/nanorod bundles. The possible reaction equations are as follows:

$$3Mn^{2+} + 2NH_4HB_4O_7 + 3H_2O \rightarrow Mn_3B_7O_{13}OH + 2NH_4^+ + 7H^+ + BO_3^{3-} \quad (1)$$

$$3Mn^{2+} + 2NH_4HB_4O_7 + 10H_2O \rightarrow 3MnBO_2OH + 2NH_4^+ + 19H^+ + 5BO_3^{3-} \quad (2)$$

Finally, the w-Mn_2OBO_3 and e-Mn_2OBO_3 were obtained after calcination, and the reaction equations are as follows:

$$4Mn_3B_7O_{13}OH + 3/2O_2 \rightarrow 6(w\text{-}Mn_2OBO_3) + 2H_2O + 11B_2O_3 \quad (3)$$

$$4MnBO_2OH + 1/2O_2 \rightarrow 2(e\text{-}Mn_2OBO_3) + 2H_2O + B_2O_3 \quad (4)$$

A schematic illustration of the formation of w-Mn_2OBO_3 and e-Mn_2OBO_3 is shown in Scheme 1. In addition, it was found that only MnOOH nanowires or $MnBO_2OH$ nanorods could be obtained using either water or ethanol as a solvent if H_3BO_3 was used as borate reagent instead of $NH_4HB_4O_7{\cdot}3H_2O$ while keeping other reaction conditions unchanged (Fig. S4, in the ESM).

Figures 4(a) and 4(d), respectively, demonstrate the discharge–charge curves of the electrodes made from the $Mn_3B_7O_{13}OH$ nanorods and the $MnBO_2OH$ nanorod bundles at a current density of 100 $mA{\cdot}g^{-1}$ at room temperature in the potential window between 0.01 and 3.0 V (vs. Li^+/Li). The initial discharge capacities of the $Mn_3B_7O_{13}OH$ and $MnBO_2OH$ are 810 and 855 $mAh{\cdot}g^{-1}$, with values of 538 and 507 $mAh{\cdot}g^{-1}$ retained after 50 cycles, respectively. The cycling performances of the $Mn_3B_7O_{13}OH$ nanorods and the $MnBO_2OH$ nanorod bundles are shown in Figs. 4(b) and 4(e). Both the samples showed good capacity retention and stability. In addition, the rate performances of the $Mn_3B_7O_{13}OH$ and $MnBO_2OH$ were also tested at various current densities, and displayed

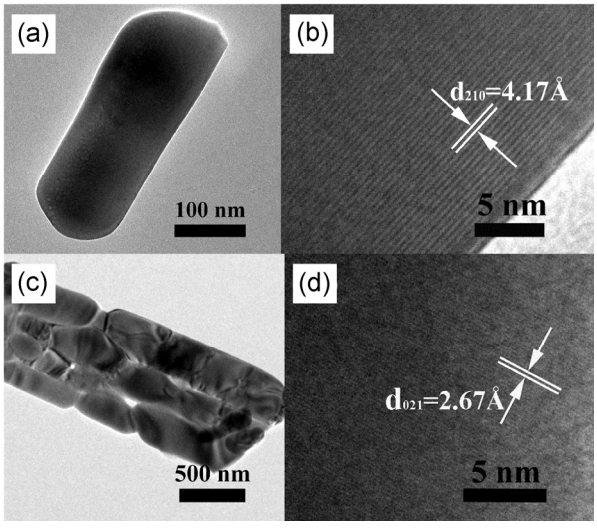

Figure 3 HRTEM images of part of a randomly selected (a, b) w-Mn_2OBO_3 and (c, d) e-Mn_2OBO_3 nanorod.

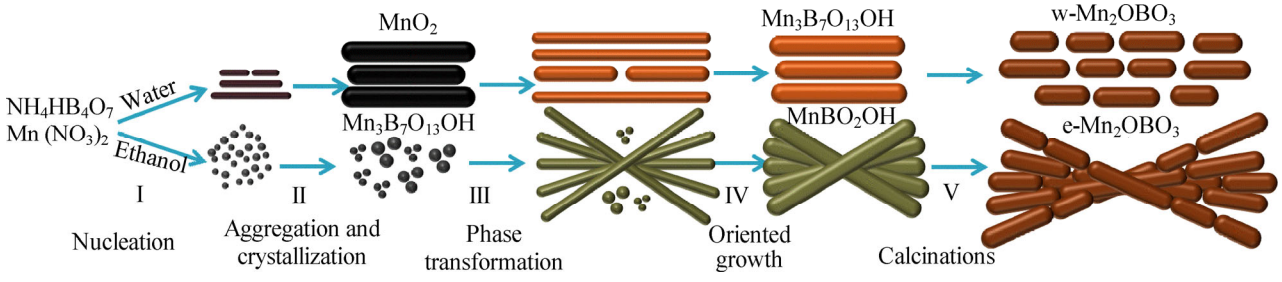

Scheme 1 Schematic Illustration of the formation of w-Mn_2OBO_3 and e-Mn_2OBO_3.

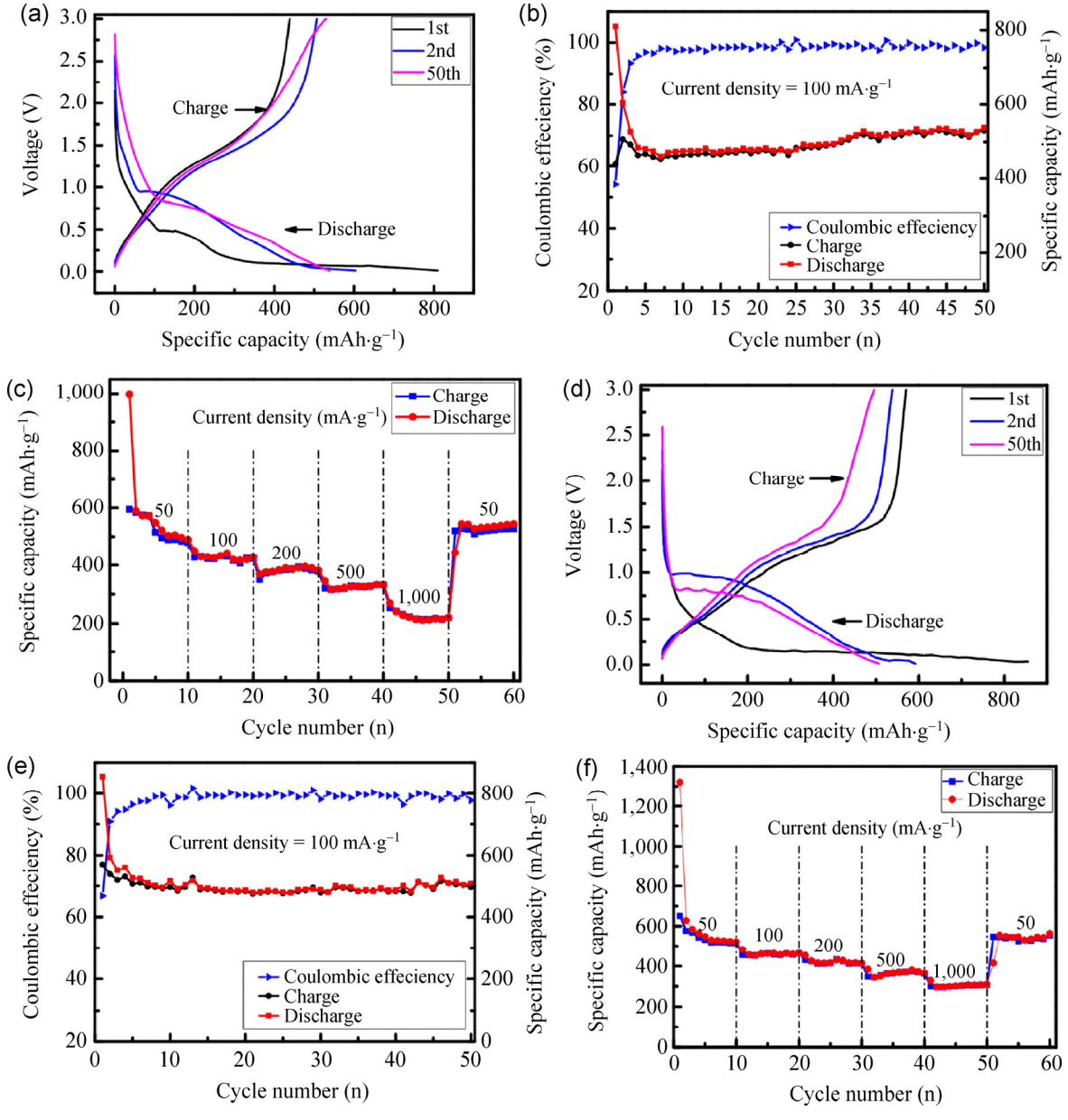

Figure 4 Discharge–charge curves and cycle performance of (a, b) $Mn_3B_7O_{13}OH$ and (d, e) $MnBO_2OH$ at a current density of 100 mA·g^{-1}; rate performance of (c) $Mn_3B_7O_{13}OH$ and (f) $MnBO_2OH$ at 50, 100, 200, 500, 1,000 mA·g^{-1}.

high reversibility [Figs. 4(c) and 4(f)]. Details of the capacities and coulombic efficiencies of the cycling and rate performances of the products are shown in Table 1.

The discharge–charge voltage profiles of the w-Mn_2OBO_3 nanorods and e-Mn_2OBO_3 nanorod bundle electrodes under the same conditions as the manganese borate hydroxides are illustrated in Fig. 5(a). The initial discharge capacities of w-Mn_2OBO_3 and e-Mn_2OBO_3 are 1,172 and 1,037 mAh·g^{-1}, respectively, values which are higher than those of the $Mn_3B_7O_{13}OH$ and $MnBO_2OH$ (Fig. 5(a)). However they suffer from large irreversible capacity loss, which is common in other borates and some transition metal oxide anodes [4–6, 17–23]. According to the literature, the high irreversible capacity loss generally observed in the first cycle for borate materials can be largely attributed to the occurrence of side reactions involving electrolyte oxidation with the formation of a solid electrolyte interphase (SEI) film during the first discharge process [24]. An ex situ lithiation process (by directly contacting a lithium metal foil with the w-Mn_2OBO_3 (or e-Mn_2OBO_3) electrode and then dipping both of them into the electrolyte for 30 min) was carried out and can be considered to be a surface pretreatment process, which could pre-form the SEI before the subsequent cycling processes [25, 26]. As a result of this process, the first cycle coulombic efficiencies of w-Mn_2OBO_3 and e-Mn_2OBO_3 increased to 77.8% and 75.3%, respectively (Fig. S5, in the ESM). In addition, it is obvious that there is a large deviation in the potential between the charge and discharge curves. This large difference may be a feature of metal oxide anode polarization related to ion transfer during charge–discharge cycles. This phenomenon is often observed in metal oxide anodes due to their poor electrical conductivity [27, 28]. The w-Mn_2OBO_3 and e-Mn_2OBO_3 products also show better LIB cycling performances than the manganese borate hydroxides at a current density of 100 mA·g^{-1} (see Fig. 5(b)). After 120 cycles, the capacities of the w-Mn_2OBO_3 and e-Mn_2OBO_3 are still maintained at 724 and 706 mAh·g^{-1}, respectively (Fig. 5(b)). The higher rate performances (2A·g^{-1}) of the w-Mn_2OBO_3 and e-Mn_2OBO_3 are shown in Fig. S6 (in the ESM). The initial capacities of w-Mn_2OBO_3 and e-Mn_2OBO_3 are 1,140 and 1,008 mAh·g^{-1}, with values of 353.4 and 315.6 mAh·g^{-1} retained after 100 cycles, respectively. In addition, the capacity of e-Mn_2OBO_3 exceeds that of w-Mn_2OBO_3 as cycle number increases. The reasons for the distinctly higher capacity of w-Mn_2OBO_3 compared with that of e-Mn_2OBO_3 in the starting cycling stage may be attributed to the smaller particle size (which can provide more active sites), shorter Li-ion insertion length and less agglomeration of w-Mn_2OBO_3 compared with e-Mn_2OBO_3 [29]. The w-Mn_2OBO_3 electrode has lower electronic resistance (Re) and charge-transfer resistance (Rct) values but a larger diffusion coefficient (D) than the corresponding values for the e-Mn_2OBO_3 before cycling, which indicates it affords higher mobility for Li^+ ion diffusion [30]. Even when the batteries were cycled at a current density of 2 A·g^{-1} for 10 cycles, the 1D characteristics of the w-Mn_2OBO_3 and e-Mn_2OBO_3 were still retained (Fig. S9, in the ESM) but the nanorod sizes changed to some extent. For example, some of the e-Mn_2OBO_3 nanorods cracked into smaller sized nanorods. However, when the w-Mn_2OBO_3 and e-Mn_2OBO_3 were evaluated as half cell electrodes after 120 cycles at a current density of 100 mA·g^{-1}, the corresponding values of Re, Rct,

Table 1 Capacities and coulombic efficiencies during cycling and rate performances of the products

Sample	Initial discharge/charge capacity (mAh·g^{-1})	Discharge /charge capacity (mAh·g^{-1})	Initial coulombic efficiency (%)	Coulombic efficiency (%)	Rate performance—discharge capacities (mAh·g^{-1}) at various current densities (mA·g^{-1})					
					50	100	200	500	1,000	50
$Mn_3B_7O_{13}OH$	810/439	538/530 (50th)	54.2	98.5 (50th)	490	429	382	333	220	545
$MnBO_2OH$	855/570	507/495 (50th)	66.7	97.6 (50th)	522	465	414	365	309	563
w-Mn_2OBO_3	1,172/694	724/720 (120th)	59.2	99.4 (120th)	649	591	569	503	438	784
e-Mn_2OBO_3	1,037/580	706/701 (120th)	55.9	99.3 (120th)	506	463	421	361	321	604

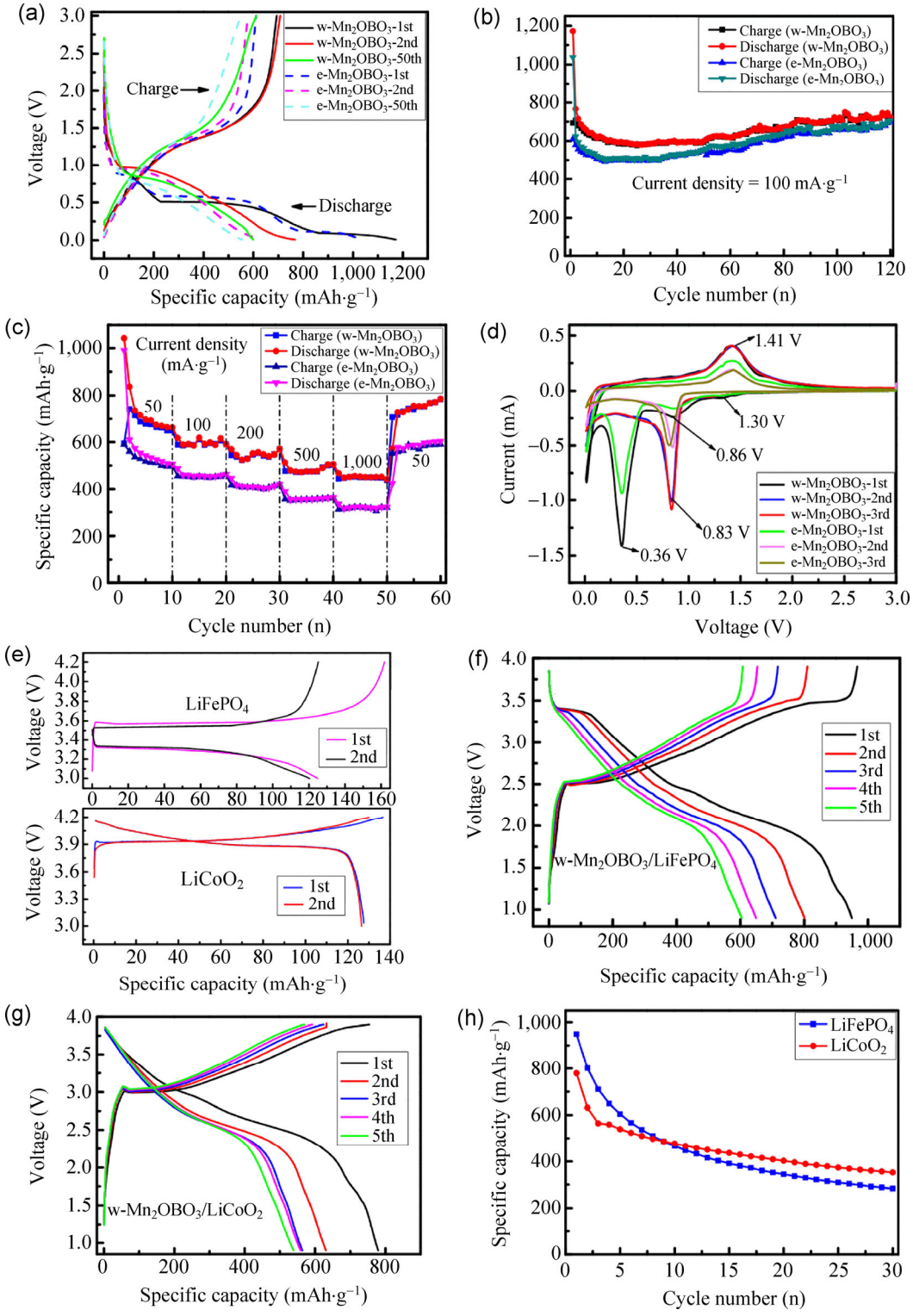

Figure 5 Electrochemical performances of the w-Mn_2OBO_3 and e-Mn_2OBO_3: (a) discharge–charge curves (b) cycle performance at a current of 100 mA·g^{-1}; (c) rate performance at 50, 100, 200, 500, 1,000 mA·g^{-1}; (d) the first three consecutive CVs of the electrodes made from w-Mn_2OBO_3 and e-Mn_2OBO_3 at a scan rate of 0.1 mV·s^{-1} in the voltage range 0.01–3.0 V versus Li^+/Li; (e) the discharge–charge curves of $LiFePO_4$ and $LiCoO_2$ versus Li^+/Li in the first two cycles at a current density of 100 mA·g^{-1} in the voltage range 3.0–4.2 V; (f) voltage profile of w-Mn_2OBO_3/$LiFePO_4$ full battery at a current density of 100 mA·g^{-1} in the voltage range 0.9–3.9 V; (g) voltage profile of w-Mn_2OBO_3/$LiCoO_2$ full battery at a current density of 100 mA·g^{-1} in the voltage range 0.9–3.9 V; (h) cycle performances of the w-Mn_2OBO_3/$LiFePO_4$ and w-Mn_2OBO_3/$LiCoO_2$ full cells at a current density of 100 mA·g^{-1}.

and D of the two materials become similar (Fig. S7 and Table S1, in the ESM). In addition, the XRD patterns and morphologies of w-Mn_2OBO_3 and e-Mn_2OBO_3 also became almost the same after 120 cycles (Fig. S8, in the ESM). As the w-Mn_2OBO_3 and e-Mn_2OBO_3 have similar structures (amorphous) and morphologies after long cycling, it is reasonable that they have almost similar electrochemical performance after 120 cycles at 100 mA·g^{-1}.

Figure 5(c) demonstrates the rate performance of w-Mn_2OBO_3 and e-Mn_2OBO_3 electrodes cycled at various current densities (50, 100, 200, 500 and 1,000 mA·g^{-1}). The capacities at the given current densities are listed in Table 1. It is obvious that the w-Mn_2OBO_3 and e-Mn_2OBO_3 electrodes displayed better stability and reversibility than the $Mn_3B_7O_{13}OH$ and $MnBO_2OH$. When the current density was reduced back to 50 mA·g^{-1}, the capacities of w-Mn_2OBO_3 and e-Mn_2OBO_3 recovered to 784 and 604 mAh·g^{-1}, respectively. The first three consecutive cyclic voltammograms (CVs) of the electrodes made from w-Mn_2OBO_3 and e-Mn_2OBO_3 were recorded (Fig. 5(d)). It is obvious that the w-Mn_2OBO_3 sample has larger curve area and higher redox peaks than those of the e-Mn_2OBO_3 sample, which is consistent with the higher capacity of the w-Mn_2OBO_3 [8]. Three reduction peaks can be found in the cathodic polarization process of the first cycle for both of the two Mn_2OBO_3 samples. The broad peak centered at 1.30 V can be attributed to the reduction of Mn^{3+} to Mn^{2+} [31], the intense peak located at 0.36 V can be assigned to the further reduction of Mn^{2+} to metallic Mn [16], while the peak centered at 0.86 V could be associated with an irreversible reaction related to the lithium ion insertion into the conductive agent acetylene black [27]. There is only one oxidation peak in the following anodic sweep. The peak located at 1.41 V is due to the oxidation of Mn to Mn^{2+}. The second cycle is characterized by a pair of redox peaks at 0.83/1.41 V, which may be attributed to the formation of a new phase. From the second cycle onwards, the CV curves are mostly overlapping, which indicates the good reversibility of the electrochemical reactions. Based on the above analysis, the lithium insertion and extraction reactions for w-Mn_2OBO_3 and e-Mn_2OBO_3 electrodes can be tentatively proposed to be as follows:

$$Mn_2OBO_3 + 5Li^+ + 5e^- \rightarrow 2Mn + Li_3BO_3 + Li_2O \quad (5)$$

However the exact lithium insertion/extraction reaction mechanism still needs further study.

Similarly, the possible electrode reactions of the two borate precursors can be tentatively written as follows [32, 33]:

$$Mn_3B_7O_{13}OH + 6Li^+ + 6e^- \rightarrow 6Mn + Li_3BO_3 + Li_2O + LiOH + 3B_2O_3 \quad (6)$$

$$MnBO_2OH + 2Li^+ + 2e^- \rightarrow Mn + 1/2Li_2O + LiOH + 1/2B_2O_3 \quad (7)$$

According to the electrochemical equation (C_0 = 26,800 n/M mAh·g^{-1}), the theoretical capacities of the $Mn_3B_7O_{13}OH$ nanorods, $MnBO_2OH$ nanorod bundles and the corresponding Mn_2OBO_3 are 345.45, 467.14 and 725.56 mAh·g^{-1}, respectively.

In terms of the LIB cycle performances and rate performances, all the four samples displayed good reversibility and stability. This can largely be attributed to the one-dimensional morphology, which can provide efficient electron transport pathways and facile strain relaxation during the battery charge and discharge processes [34–37]. In addition, the w-Mn_2OBO_3 nanorods and e-Mn_2OBO_3 nanorod bundle electrodes delivered higher capacity than that of the manganese borate hydroxides ones. This phenomenon is often observed with manganese oxide and manganite [38, 32]. A comparative experiment using tetraglycol as solvent was also undertaken and the results are shown in Fig. S10 (in the ESM).

Based on the best performance of the w-Mn_2OBO_3, a full battery composed of a w-Mn_2OBO_3 nanorod anode and a commercial $LiFePO_4$ (or $LiCoO_2$) cathode was assembled to demonstrate its practical applications. The active materials of the coin cell in our case are only composed of one disc of anode and one disc of cathode with light mass, which is different from the commercial cylindrical cell (Sony 18650G8). The capacity (mAh) of the commercial $LiFePO_4$ (or $LiCoO_2$) cathode we used is ~35% higher than the capacity (mAh) of the Mn_2OBO_3 nanorods (which means that the full coin batteries are anode-limited) and the specific capacities of the batteries refer to the mass of the loaded Mn_2OBO_3 nanorod electrodes not the total mass

of the coin cell. Therefore, the as-measured specific capacity values of the full coin batteries are different from those of the calculated ones using the formula $[(1/(1/C_{anode} + 1/C_{cathode}))]$ for the commercial cylindrical cell (Sony 18650G8) [39]. The first discharge capacity of the full battery with a $LiFePO_4$ cathode was 949.0 mAh·g^{-1} at a current density of 100 mA·g^{-1}, which is a little lower than that of the half-cell (Fig. 5(f)). The reason for the reduction in capacity may be the large internal resistance in the full battery. The w-Mn_2OBO_3 nanorod anode has an average plateau at 1.0 V (Fig. 5(a)), while the $LiFePO_4$ cathode shows a voltage value of 3.5 V with a plateau (Fig. 5(e)). The full cell operates around 2.5 V with a voltage profile matching that expected from a combination of the flat voltage of $LiFePO_4$ and w-Mn_2OBO_3. The capacity of the full battery is still 604.4 mAh·g^{-1} after five cycles. In the other full cell system where $LiCoO_2$ was utilized as the cathode and w-Mn_2OBO_3 as the anode, the full cell displays a voltage platform at ~3.0 V, which is consistent with the plateau of 1.0 V (w-Mn_2OBO_3) and 3.9 V ($LiCoO_2$). The initial capacity of the full cell was 779 mAh·g^{-1}, with a value of 539.1 mAh·g^{-1} retained after five cycles (Fig. 5(g)). Although the first five capacities are lower, the long cycling performance of the w-Mn_2OBO_3/$LiCoO_2$ full cell is better than that of w-Mn_2OBO_3/$LiFePO_4$. After 30 cycles at a current density of 100 mA·g^{-1}, the capacity retention efficiency of w-Mn_2OBO_3/$LiCoO_2$ is 45.14%, which is much higher than the corresponding value of 29.86% for w-Mn_2OBO_3/$LiFePO_4$ (Fig. 5(h)). To the best of our knowledge, this is the first study where a Mn_2OBO_3 anode has been assembled into a full cell. The excellent performance of the full cell indicates the promising practical applications of w-Mn_2OBO_3 in the future.

4 Conclusions

A novel and facile solution-based method has been utilized to synthesize one-dimensional manganese borate hydroxides using different solvents. After calcination, the $Mn_3B_7O_{13}OH$ nanorods and $MnBO_2OH$ nanorod bundles can be conveniently converted into Mn_2OBO_3 nanorods/nanorod bundles while their shapes are retained. The smaller w-Mn_2OBO_3 nanorods showed better electrode performance than the larger e-Mn_2OBO_3 nanorod bundles. The different surface area, more active sites, shorter diffusion lengths for lithium insertion/extraction and lower resistance of the w-Mn_2OBO_3 nanorods are responsible for its higher capacity, better stability and longer cycling life-time. The performance of w-Mn_2OBO_3 in a full battery is also very attractive. The promising electrochemical performance of the products, especially 1D Mn_2OBO_3, evidences their promise for application as anodes for LIBs.

Acknowledgements

This work was supported by the 973 Project of China (No. 2011CB935901), the National Natural Science Foundation of China and the Chinese Academy of Sciences Large Apparatus United Fund (Nos. 11179043 and 21471091).

Electronic Supplementary Material: Supplementary material is available in the online version of this article at http://dx.doi.org/10.1007/s12274-014-0669-7.

References

[1] Reddy, M. V.; Subba Rao, G. V.; Chowdari, B. V. R. Metal oxides and oxysalts as anode materials for Li ion batteries. *Chem. Rev.* **2013**, *113*, 5364–5457.

[2] Gong, Z. L.; Yang, Y. Recent advances in the research of polyanion-type cathode materials for Li-ion batteries. *Energy Environ. Sci.* **2011**, *4*, 3223–3242.

[3] Rowsell, J. L. C.; Gaubicher, J.; Nazar, L. F. A new class of materials for lithium-ion batteries: Iron (III) borates. *J. Power Sources* **2001**, *97*, 254–257.

[4] Rowsell, J. L. C.; Nazar,L. F. Synthesis, structure, and solid-state electrochemical properties of Cr_3BO_6: Anew chromium (III) borate with the norbergite structure. *J. Mater. Chem.* **2001**, *11*, 3228–3233.

[5] Okada, S.; Tonuma, T.; Uebo, Y.; Yamaki, J. I. Anode properties of calcite-type MBO_3 (M: V, Fe). *J.Power Sources* **2003**, *119*, 621–625.

[6] Débart, A.; Revel, B.; Dupont, L.; Montagne, L.; Leriche, J. B.; Touboul, M.; Tarascon, J. M. Study of the reactivity mechanism of $M_3B_2O_6$ (with M= Co, Ni, and Cu) toward lithium. *Chem. Mater.* **2003**, *15*, 3683–3691.

[7] Wang, T. Y.; Peng, Z.; Wang, Y. H.; Tang, J.; Zheng, G.F. MnOnanoparticle@ mesoporouscarbon composites grown on

conducting substrates featuring high-performance lithium-ion battery, supercapacitorand sensor. *Sci. Rep.* **2013**, *3*, 2693.

[8] Chang, L.; Mai, L. Q.; Xu, X.; An,Q. Y.; Zhao,Y. L.; Wang, D. D.; Feng, X. Pore-controlled synthesis of Mn_2O_3 microspheres for ultralong-life lithium storage electrode. *RSC Adv.* **2013**, *3*, 1947–1952.

[9] Li, L. H.; Nan, C. Y.; Lu, J.; Peng, Q.; Li, Y. D. α-MnO_2 nanotubes: high surface area and enhanced lithium battery properties. *Chem. Commun.* **2012**, *48*, 6945–6947.

[10] Du, J.; Gao, Y. Q.; Chai, L. L.; Zou, G. F.; Li, Y.; Qian, Y.T. Hausmannite Mn_3O_4nanorods: Synthesis, characterization and magnetic properties. *Nanotech.* **2006**, *17*, 4923.

[11] Fernandes, J. C.; Sarrat, F. S.; Guimaraes, R. B.; Freitas, R. S.; Continentino, M. A.; Doriguetto, A. C.; Mascarenhas, Y. P.; Ellena, J.; Castellano, E. E.; Tholence, J. L. et al. Structure and magnetism of $MnMgB_2O_5$ and $Mn_2B_2O_5$. *Phys. Rev. B* **2003**, *67*, 104413.

[12] Continentino, M. A.; Pedreira, A. M.; Guimaraes, R. B.; Mir, M.; Fernandes, J. C.; Freitas, R. S.; Ghivelder, L. Specific heat and magnetization studies of Fe_2OBO_3, Mn_2OBO_3, and $MgScOBO_3$. *Phys. Rev. B* **2001**, *64*, 014406.

[13] Goff, R. J.; Williams, A. J.; Attfield, J. P. Spin, charge, and orbital order in Mn_2OBO_3. *Phys. Rev. B*, **2004**, *70*, 014426.

[14] Li, S. L.; Xu, L. Q.; Zhai, Y. J.; Yu, H. X. Co-pyrolysis synthesis of Fe_3BO_6nanorods as high performance anodes for lithium-ion batteries. *RSC Adv.* **2014**, *4*, 8245–8249.

[15] Norrestam, R.; Kritikos, M.; Sjödin, A. Manganese (II, III) oxyborate, Mn_2OBO_3: A distorted homometallicwarwickite—synthesis, crystal structure, band calculations, and magnetic susceptibility. *J. Solid State Chem.* **1995**, *114*, 311–316.

[16] Rivas-Murias, B.; Rivadulla, F.; Sánchez-Andújar, M.; Castro-Couceiro, A.; Señarís-Rodríguez, M. A.; Rivas, J. Role of t(2g) versus e(g) interactions in the physical properties of A(2)OBO(3) (A = Mn, Fe). *Chem. Mater.* **2006**, *18*, 4547–4552.

[17] Wang, Z. Y.; Luan, D. Y.; Boey, F. Y. C.; Lou, X. W. Fast formation of SnO_2 nanoboxes with enhanced lithium storage capability. *J. Am. Soc.* **2011**, *133*, 4738–4741.

[18] Guo, C. X.; Wang, M.; Chen, T.; Lou, X. W.; Li, C. M. A hierarchically nanostructured composite of MnO_2/conjugated polymer/graphene for high-performance lithium ion batteries. *Adv. Energy Mater.* **2011**, *1*, 736–741.

[19] Zhang, R. R.; He, Y. Y.; Li, A. H.; Xu, L. Q. Facile synthesis of one-dimensional Mn_3O_4/Zn_2SnO_4 hybrid composites and their high performance as anodes for LIBs. *Nanoscale* **2014**, *6*, 14221–14226.

[20] Zhang, R. R.; He, Y. Y.; Xu, L. Q. Controllable synthesis of hierarchical $ZnSn(OH)_6$ and Zn_2SnO_4 hollow nanoshperes and their applications as anodes for lithium ion batteries. *J. Mater. Chem. A* **2014**, *2*, 17979–17985.

[21] Li, S. L.; Li, A. H.; Zhang, R. R.; He, Y. Y.; Zhai, Y. J.; Xu, L. Q. Hierarchical porous metal ferrite ball-in-ball hollow spheres: general synthesis, formation mechanism, and high performance as anode materials for Li-ion batteries. *Nano Res.* **2014**, *7*, 1116–1127.

[22] Li, L.; Kovalchuk, A.; Tour, J. M. SnO_2-reduced grphene oxide nanoribbons as anodes for lithium ion batteries with enhanced cycling stability. *Nano Res.* **2014**, *7*, 1319–1326.

[23] Xia, H.; Xiong, W.; Lim, C. K.; Yao, Q. F.; Wang, Y. D.; Xie, J. P. Hierarchical TiO_2-B nanowire@α-Fe_2O_3nanothorn core-branch arrays as superior electrodes for lithium-ion microbatteries. *Nano Res.* **2014**. (DOI: 10.1007/s12274-014-0539-3)

[24] Hu, L.; Zhong, H.; Zheng, X. R.; Huang, Y. M.; Zhang P.; Chen, Q. W. $CoMn_2O_4$ spinel hierarchical microspheres assembled with porous nanosheets as stable anodes for lithium-ion batteries. *Sci. Rep.* **2012**, *2*, 986.

[25] Hassoun, J.; Bonaccorso, F.; Agostini, M.; Angelucci, M.; Betti, M. G.; Cingolani, R.; Gemmi, M.; Mariani, C.; Panero, S.; Pellegrini, V. et al. An advanced lithium-ion battery based on a graphene anode and a lithium iron phosphate cathode. *Nano Lett.* **2014**, *14*, 4901–4906.

[26] Hassoun, J.; Lee, K. S.; Sun, K. Y.; Scrosati, B. An advanced lithium ion battery based on high performance electrode materials. *J. Am. Chem. Soc.* **2011**, *133*, 3139–3143.

[27] Mai, Y. J.; Shi, S. J.; Zhang, D.; Lu, Y.; Gu, C. D.; Tu, J. P. NiO-graphene hybrid as an anode material for lithium ion batteries. *J. Power Sources* **2012**, *204*, 155–161.

[28] Mai, Y. J.; Xia, X. H.; Chen, R.; Gu, C. D.; Wang, X. L.; Tu, J. P. Self-supported nickel-coated NiO arrays for lithium-ion batteries with enhanced capacity and rate capability. *Electrochim. Acta* **2012**, *67*, 73–78.

[29] Qiu, Y. C.; Xu, G. L.; Yan, K. Y.; Sun, H.; Xiao, J. W.; Yang, S. H.; Sun, S. G.; Jin, L. M.; Deng, H. Morphology-conserved transformation: synthesis of hierarchical mesoporous nanostructures of Mn_2O_3 and the nanostructural effects on Li-ion insertion/deinsertion properties. *J. Mater. Chem.* **2011**, *21*, 6346–6353.

[30] Shenouda A. Y.; Liu, H. K. Studies on electrochemical behaviour of zinc-doped $LiFePO_4$ for lithium battery positive electrode. *J. Alloys Comp.* **2009**, *477*, 498–503.

[31] Deng, Y. F.; Li, Z. E.; Shi, Z. C.; Xu, H.; Peng, F.; Chen, G. H. Porous Mn_2O_3 microsphere as a superior anode material for lithium ion batteries. *RSC Adv.* **2012**, *2*, 4645–4647.

[32] Lou, X. M.; Wu, X. Z.; Zhang, Y. X. A study about γ-MnOOH nanowires as anode materials for rechargeable Li-ion batteries. *J. Alloys Comp.* **2013**, *550*, 185–189.

[33] Lou, X. M.; Wu, X. Z.; Zhang, Y. X. Goethite nanorods as anode electrode materials for rechargeable Li-ion batteries. *Electrochem. Commun.* **2009**, *11*, 1696–1699.

[34] Kim, D. K.; Muralidharan, P.; Lee, H. W.; Ruffo, R.; Yang, Y.; Chan, C. K.; Peng, H. L.; Huggins, R. A.; Cui, Y. Spinel $LiMn_2O_4$ nanorods as lithium ion battery cathodes. *Nano Lett.* **2008**, *8*, 3948–3952.

[35] Jiang, J.; Li, Y. Y.; Liu, J. P.; Huang, X. T. Building one-dimensional oxide nanostructure arrays on conductive metal substrates for lithium-ion battery anodes. *Nanoscale* **2011**, *3*, 45–58.

[36] Jiang, J.; Li, Y. Y.; Liu, J. P.; Huang, X. T.; Yuan, C. Z.; Lou, X. W. Recent advances in metal oxide-based electrode architecture design for electrochemical energy storage. *Adv. Mater.* **2012**, *24*, 5166–5180.

[37] Jiang, J.; Luo, J. S.; Zhu, J. H.; Huang, X. T.; Liu, J. P.; Yu, T. Diffusion-controlled evolution of core-shell nanowire arrays into integrated hybrid nanotube arrays for Li-ion batteries. *Nanoscale* **2013**, *5*, 8105–8113.

[38] Zhang, X.; Qian, Y. T.; ZhuY. C.; Tang, K. B. Synthesis of Mn_2O_3 nanomaterials with controllable porosity and thickness for enhanced lithium-ion batteries performance. *Nanoscale* **2014**, *6*, 1725–1731.

[39] Yoshio, M.; Tsumura, T.; Dimov, N. Electrochemical behaviors of silicon based anode material. *J. Power Sources* **2005**, *146*, 10–14.